Experimental study of the magnetic phase diagrams of DyCu

M Amara†, P Morin† and F Bourdarot‡

† Laboratoire Louis-Néel§, CNRS, BP 166X, 38042 Grenoble Cédex, France
‡ Magnétisme et Diffraction Neutronique, DRF/MC, Centre d'Etudes Nucléaires, BP 85X, 38041 Grenoble Cédex, France

Abstract. DyCu (CsCl-type) orders antiferromagnetically at $T_N = 62$ K. By measuring magnetization curves, the (H, T) phase diagrams are established for magnetic fields applied along fourfold and threefold axes. On the basis of neutron diffraction experiments on single crystals, magnetic structures are associated with each of the phases seen. The spontaneous and field-stabilized structures are multiaxial, with moments pointing along threefold or twofold directions. The phase sequence in the ordered range of DyCu reveals antiferroquadrupolar couplings of trigonal symmetry.

1. Introduction

Rare-earth intermetallic compounds present a large variety of magnetic structures, which result from the complex coexistence of two-ion and one-ion interactions [1]. In low-symmetry antiferromagnetic compounds, the crystalline-electric-field (CEF) anisotropy and the RKKY-type bilinear interactions generally determine a unique magnetic structure. In contrast, in high-symmetry lattices, the magnetic ground state would be highly degenerate if just these two couplings were considered. The actual structure is determined by high-order pair interactions, the most important ones being established to be of quadrupolar type [2]. These quadrupolar interactions are large for the cubic rare-earth compounds RAg, RCu, RCd, and RZn, which have the CsCl-type structure. For TmZn the quadrupolar interactions are strong enough to drive a quadrupolar ordering in the paramagnetic phase [3], but in most cases these couplings are dominated by the bilinear ones. Nevertheless, these quadrupolar couplings are active in selecting the most energetically favourable structure [4]. The observation of magnetic multiaxial (multi-k) structures, i.e. with moments pointing from site to site along different equivalent axes, is then related to a dispersion curve of quadrupolar pair interactions having its extremum outside the zone centre. The case of the NdZn compound has particularly well illustrated the interest of this approach [5, 6]. From an experimental point of view these multiaxial structures are hard to find evidence for, since they are indistinguishable from the collinear structures investigated when using powder neutron diffraction [7]. Studies on single crystals under an applied magnetic field, taking account of the many possible domains, are then necessary [8, 5].

The CsCl-type compound DyCu orders antiferromagnetically at $T_N = 62$ K. Its neutron powder diffraction pattern is analysed using propagation vectors from the $\langle 1/2\ 1/2\ 0 \rangle$ star

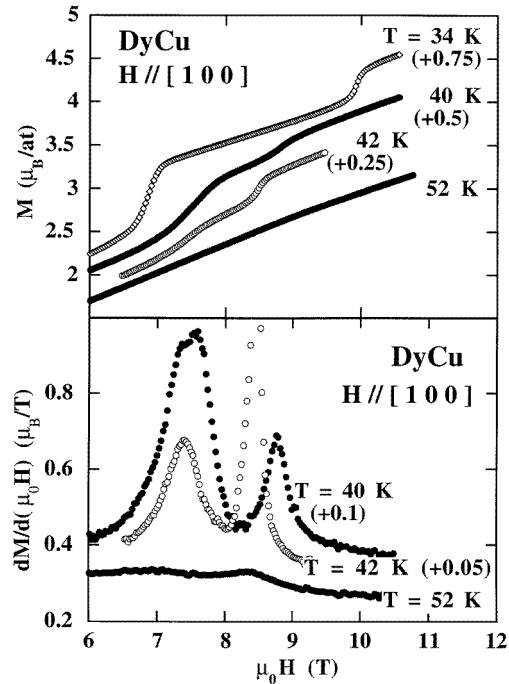§ Associated with the University Joseph-Fourier of Grenoble.

Figure 1. Upper part: isothermal magnetization processes along the [1 0 0] direction at $T = 52, 42, 40$, and 34 K. Lower part: field derivatives of the $T = 52, 42$, and 40 K magnetization curves. The curves are shifted along the vertical axis according to the values given in brackets.

[9]. From CEF analysis, which favours threefold axes as directions of easy magnetization, and in view of the absence of any evident strain below T_N, the spontaneous magnetic structure has been proposed as being a triple-k one, the spins pointing along threefold axes [10].

In order to extend the knowledge of the magnetic properties of DyCu, we have investigated its ordered range by means of magnetization and neutron diffraction measurements on single crystals, for magnetic fields applied along the [0 0 1], [1 1 1], and, to a lesser extent, [1 1 0] axes. As the main results, we present first the magnetic phase diagrams obtained, and second the magnetic structures associated with each of the phases identified.

2. Magnetization measurements

Most of the magnetization measurements have been performed at the Laboratoire Louis-Néel by the extraction method in two cryomagnets with maximum applied fields of 7.6 and 16 T. Additional measurements were also done at the High Magnetic Fields Laboratory in Grenoble, up to 27 T. The temperature range of the measurements extends from 1.5 K to room temperature. The single crystals used were cut from an ingot prepared by the Bridgman technique in sealed tantalum crucibles. Isothermal and isofield measurements have been carried out for the three main crystallographic directions. Isothermal magnetization curves are particularly well suited for locating the transition lines displaying weak slopes on the

(H, T) phase diagram, while the isofield curves are ideal for the nearly vertical lines. To achieve a better accuracy in locating the transition points, the field or temperature numerical derivatives of the magnetization have been used. The first-order transitions are located where the derivative is a maximum, and the second-order transition is located at the mid-point of the jump of the derivative. In the case of the paramagnetic–antiferromagnetic transition, this last definition has the advantage that it can be applied over the whole magnetic field range; experimentally, the magnetization curve always displays a change of slope at the transition temperature, whereas there is a maximum of M only for low values of the magnetic field.

2.1. Magnetization along the [0 0 1] axis

For temperatures just below $T_N = 63$ K, the magnetization curves are nearly linear, as a result of a very weak anisotropy (figure 1, upper part). However, further detail can be added to this first view using the field derivative of the magnetization (figure 1, lower part). At $T = 52$ K two transitions can be resolved below $\mu_0 H = 11$ T, one as a peak at $\mu_0 H = 8.4$ T, and the other as a wide bump at about $\mu_0 H = 7$ T. On reducing the temperature, the amplitude of the anomalies is increased; two peaks can be easily identified on the derivative of the $T = 42$ K magnetization curve. At $T = 40$ K, the $\mu_0 H = 7.5$ T field-derivative peak has a double structure resulting from two very close transitions. At even lower temperatures, the transitions clearly appear as steps in the magnetization curves: two successive transitions are observed for temperatures lower than 40 K. The associated magnetization jumps are of about 2 μ_B in the low-temperature range. From reference [10], at $\mu_0 H = 20$ T, the magnetization is less than 6 μ_B, indicating that the final critical field, before the paramagnetic state, has not yet been reached.
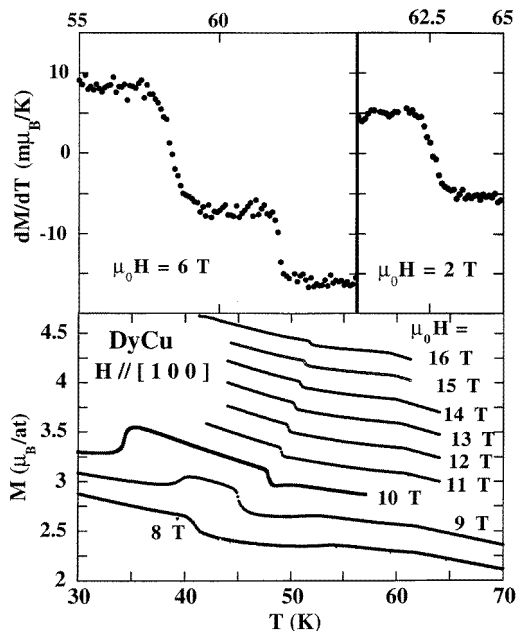

Figure 2. Lower part: isofield magnetization curves for various values of the magnetic field applied along [1 0 0]. Upper part: thermal derivatives of the $\mu_0 H = 2$ T and $\mu_0 H = 6$ T isofield magnetization curves.

Also important for establishing the magnetic phase diagram are the constant-field magnetization curves and their derivatives (figure 2). While decreasing the temperature, the first anomaly, a change of slope for the magnetization, indicates the transition towards magnetic order. The derivative of the $\mu_0 H = 2$ T curve gives a good estimate of the T_N-value, and, showing no peak but a simple step, attests to the second-order nature of the magnetic transition. At higher fields, the system shows more intricate aspects. For example, at $\mu_0 H = 6$ T, above $T = 55$ K, additional transitions can be identified through changes in the magnetization slope. The $\mu_0 H = 8$ T curve provides evidence for three transitions, the one occurring at the lower temperature ($T = 41$ K) being associated with a magnetization step. At $\mu_0 H = 9$ T (and also $\mu_0 H = 10$ T), not less than four transitions can be observed as two changes of slope and two steps. For fields equal to or higher than $\mu_0 H = 11$ T and above $T = 40$ K, two successive transitions provide the outline of a phase which could not be identified in previous measurements [11].
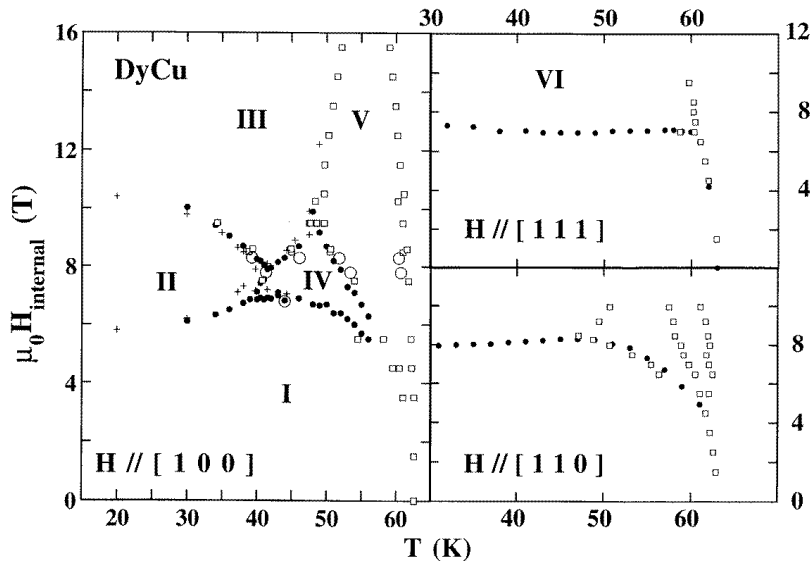

Figure 3. Magnetic phase diagrams along the main crystallographic axes in DyCu. Open squares and black dots correspond to constant-field and constant-temperature magnetization measurements, respectively. Crosses correspond to data from reference [10], and circles to neutron diffraction measurements.

The phase diagram resulting from this series of measurements is plotted in figure 3 (left-hand panel). Five different phases have been identified within the magnetic order range, and will be referred to using Roman numerals in the following.

2.2. Magnetization along the [1 1 1] axis

Along the threefold direction, both constant-field and constant-temperature magnetization curves have been measured, for fields less than $\mu_0 H = 11$ T. The isothermal magnetization processes (figure 4, upper part) present one single step for all accessible temperatures. For $T = 8$ K, above the critical field $\mu_0 H_c = 8$ T, the amplitude of the magnetization reaches approximately half of the free-Dy-ion moment (i.e. 5.3 μ_B). While increasing the temperature, the amplitude of the magnetization jump is progressively reduced, and

is nearly zero on reaching values near to T_N (see in figure 4, lower part, the field derivative of the $T = 60$ K magnetization curve). Surprisingly, the associated critical field appears to be almost unaffected by the temperature. This is rather unexpected behaviour for H_c, since in most antiferromagnets such critical fields tend to decrease with the temperature, in which they simply follow the temperature dependence of the order parameter.
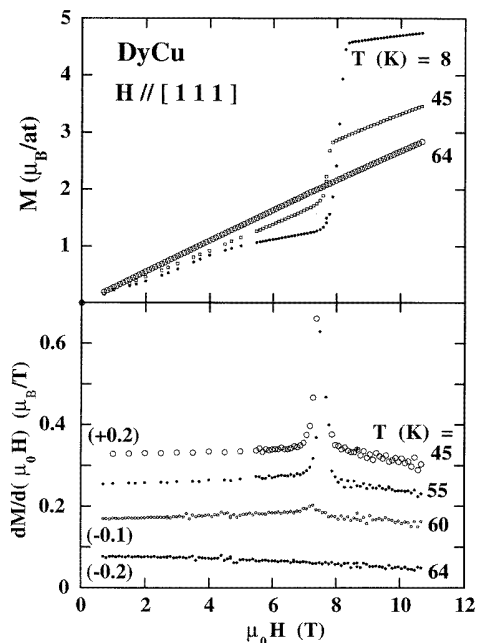

Figure 4. Upper part: isothermal magnetization processes along the [1 1 1] direction at $T = 64$, 45, and 8 K. Lower part: field derivatives of the $T = 64$, 60, 55, and 45 K magnetization curves. The values in brackets indicate shifts of the origin along the vertical axis.
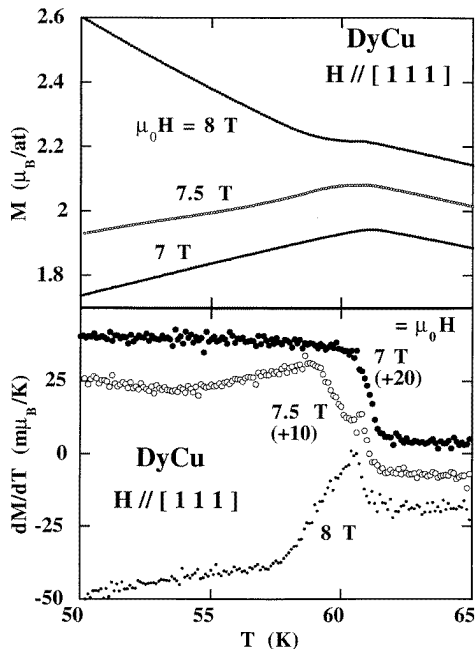
Figure 5. Upper part: isofield magnetization curves for three values of the magnetic field applied along [1 1 1]. Lower part: temperature derivatives of the $\mu_0 H_{ext} = 7$, 7.5, and 8 T isofield magnetization curves. The values in brackets indicate shifts of the origin along the vertical axis.

The isofield measurements (figure 5) show very simple thermal dependence of the magnetization. For fields below H_c, a clear change of slope, which becomes positive below T_N, reveals the entrance into the magnetic order range. For a magnetic field $\mu_0 H = 7.5$ T, very near to H_c, two kinks can be distinguished instead of one, indicating a slight downwards curvature for the line separating the spontaneous phase from the field-induced one. For fields slightly above H_c, one still observes a change of slope as the paramagnetic–magnetic border is crossed, but in contrast with what occurs below H_c, no change in sign is observed for the slope, and the curve gets steeper below T_N.

As shown in figure 3, the resulting H–T phase diagram for the threefold direction of the applied magnetic field exhibits only two (accessible) phases.

Analogous measurements have been carried out for a twofold direction of the applied magnetic field. They reveal a situation intermediate (figure 3) between the ones observed for the fourfold and threefold directions of the field. Four different phases are evident for fields less than $\mu_0 H = 11$ T.

3. Neutron diffraction experiments

The neutron diffraction experiments were at first carried out on the DN3 spectrometer (double axis with a moving up counter), at the CEN Grenoble reactor, Siloé. Subsequent measurements were done at the ILL on the D15 diffractometer. In both cases, the cryomagnet used could provide magnetic fields up to $\mu_0 H = 10$ T at variable temperature. Two samples were used for the measurements, one for each direction ([0 0 1] or [1 1 1]) of the field. In order to reduce the absorption problems due to Dy, the samples were both cut in a $1 \times 1 \times 8$ mm needle shape, with its axis along the [0 0 1] or [1 1 1] crystallographic direction. Due to the narrow gap of the cryomagnet, aiming to keep accessible the maximum number of reflections, short neutron wavelengths have been used: $\lambda = 0.993$ Å on DN3 and $\lambda = 0.8$ Å on D15. The respective $\lambda/2$ harmonic contributions to the intensities were evaluated from the nuclear [$m/2$ $n/2$ $p/2$] reflections, and included in the computed intensities.

In order to determine the magnetic structures, a large set of integrated intensities were collected for each of the phases investigated. These intensities were then compared with the ones resulting from models of structures. The theoretical intensities were computed using apparatus constants derived from nuclear intensities, which were measured at zero magnetic field, above or below T_N. The magnetic form factors used for the Dy^{3+} ion are those calculated by Stassis *et al* [12]. For the field-induced structures, a parameter describing the distortion of the structure through a change in the ferromagnetic component is introduced in the refinements. For each model tested, the procedure determines the different magnetic domains which must be considered, with their relative proportions as parameters for minimizing the reliability factor [13]:

$$R = \left(1 \Big/ \sum_i P_i\right) \sum_i P_i \left[\frac{|I_{calc} - I_{meas}|}{I_{meas}}\right]_i$$

where P_i is the inverse of the statistical error of the intensity (I_{meas}) measured for the ith reflection. The computed intensity I_{calc} results from a summation over the n domains, and can be written for a magnetic diffusion vector $\boldsymbol{H}$ associated with the antiferromagnetic propagation vector $\boldsymbol{k}$ as

$$I_{calc}(\boldsymbol{H}) = C_{app} \sum_{j=1,n} r_j (C_{magn} f((\sin\theta)/\lambda) M_{\boldsymbol{k}j} \sin(\boldsymbol{H}, \boldsymbol{M}_{\boldsymbol{k}j}))^2 + p_{\lambda/2} I_{calc}(2\boldsymbol{H})$$

where C_{app} is the apparatus constant (determined from the nuclear intensities), r_j the volume ratio of the jth domain, $C_{magn} \approx 0.569 \times 10^{-12}$ cm the magnetic diffusion constant, $f((\sin\theta)/\lambda)$ the magnetic form factor, $\boldsymbol{M}_{\boldsymbol{k}j}$ the magnetic Fourier component propagated by $\boldsymbol{k}$ in the jth domain, and $p_{\lambda/2}$ the effective flux ratio between the second and first harmonics of the monochromator. The second-harmonic contribution to the intensity here comes from a nuclear reflection, potentially enhanced by a ferromagnetic contribution, but not by higher harmonics, which can be neglected.

As no other propagation vectors except the $\langle 1/2\ 1/2\ 0 \rangle$ branches, associated for the field-induced structures with the [0 0 0] ferromagnetic propagation vector, have been observed, the search was restricted to high-symmetry structures based on the $\langle 1/2\ 1/2\ 0 \rangle$ propagation star (i.e. models of structures with moments of constant amplitude frozen along only one family of high-symmetry directions), according to the method previously used for NdZn [5].

In the case of spontaneous structures, the complete set of high-symmetry models has already been established for the $\langle 1/2\ 0\ 0 \rangle$ star, and extended to the $\langle 1/2\ 1/2\ 0 \rangle$ one [4]. Unlike in the $\langle 1/2\ 0\ 0 \rangle$ case, four magnetic Fourier components, associated with the zone centre and the three branches of the $\langle 1/2\ 1/2\ 0 \rangle$ star, can coexist within field-induced

Table 1. The Fourier description of the magnetic structures associated with the phases observed for a fourfold direction of the field. The first column gives the conditions of the neutron diffraction measurements and, in parentheses, the number of measured reflections. The labels refer to the real-space structures represented in figure 6. The fourth to sixth columns give respectively the number of domains involved in the refinement (N_{dom}), the reliability factor (R), and the amplitude of the moments ($|S|$). The seventh column gives the magnetization computed using $|S|$ for a rigid structure. The last column refers to the type of quadrupolar interaction compatible with the structure.

Phase	Magnetic structure		Label	N_{dom}	R (%)	$|S|$ (μ_B)	M (μ_B)	Inter-actions
I $T = 10$ K $H = 0$ (28)	$M_1 = [1/\sqrt{3}\ 0\ 0]$ $M_2 = [0\ 1/\sqrt{3}\ 0]$ $M_3 = [0\ 0\ 1/\sqrt{3}]$	$k_1 = [0\ 1/2\ 1/2]$ $k_2 = [1/2\ 0\ 1/2]$ $k_3 = [1/2\ 1/2\ 0]$	I_t	1	6.9	9.4 ± 0.2	0	AFQ ε
II $T = 2$ K $\mu_0 H = 7.5$ T (28)	$M_0 = [0\ 0\ 1/2\sqrt{3}]$ $M_1 = [1/\sqrt{3}\ 0\ 1/2\sqrt{3}]$ $M_2 = [0\ 0\ -1/2\sqrt{3}]$ $M_3 = [0\ 1/\sqrt{3}\ 1/2\sqrt{3}]$	$k_0 = [0\ 0\ 0]$ $k_1 = [1/2\ 0\ 1/2]$ $k_2 = [1/2\ 1/2\ 0]$ $k_3 = [0\ 1/2\ 1/2]$	II_t	4	8.1	9.3 ± 0.2	2.7	AFQ ε
III $T = 44$ K $\mu_0 H = 8.3$ T (79)	$M_0 = [0\ 0\ 1/\sqrt{3}]$ $M_1 = [0\ 1/\sqrt{3}\ 0]$ $M_2 = [1/\sqrt{3}\ 0\ 0]$	$k_0 = [0\ 0\ 0]$ $k_1 = [0\ 1/2\ 1/2]$ $k_2 = [1/2\ 0\ 1/2]$	III_t	1	11.4	8.2 ± 0.1	4.7	AFQ ε
IV $T = 48$ K $\mu_0 H = 8.3$ T (73)	$M_0 = [0\ 1/2\sqrt{2}\ 1/2\sqrt{2}]$ $M_1 = [1/\sqrt{2}\ 0\ 0]$ $M_2 = [0\ 1/2\sqrt{2}\ -1/2\sqrt{2}]$	$k_0 = [0\ 0\ 0]$ $k_1 = [0\ 1/2\ 1/2]$ $k_2 = [1/2\ 0\ 1/2]$	IV_b	8	10.8	7 ± 0.1	2.5	AFQ ε AFQ γ
	$M_0 = [0\ 0\ 1/2\sqrt{3}]$ $M_1 = [1/\sqrt{3}\ 0\ 1/2\sqrt{3}]$ $M_2 = [0\ 0\ -1/2\sqrt{3}]$ $M_3 = [0\ 1/\sqrt{3}\ 1/2\sqrt{3}]$	$k_0 = [0\ 0\ 0]$ $k_1 = [0\ 1/2\ 1/2]$ $k_2 = [1/2\ 1/2\ 0]$ $k_3 = [1/2\ 0\ 1/2]$	IV_t	4	14.6	6.1 ± 0.1	1.8	AFQ ε
V $T = 53$ K $\mu_0 H = 8.3$ T (79)	$M_0 = [0\ 0\ 1/\sqrt{3}]$ $M_1 = [1/\sqrt{3}\ 0\ 0]$ $M_2 = [0\ 1/\sqrt{3}\ 0]$	$k_0 = [0\ 0\ 0]$ $k_1 = [0\ 1/2\ 1/2]$ $k_2 = [1/2\ 0\ 1/2]$	V_t	1	11.3	5.8 ± 0.1	3.3	AFQ ε
	$M_0 = [0\ 0\ 1/\sqrt{2}]$ $M_1 = [1/\sqrt{2}\ 0\ 0]$	$k_0 = [0\ 0\ 0]$ $k_1 = [0\ 1/2\ 1/2]$	V_b	2	11.3	6.7 ± 0.1	4.7	AFQ ε FQ γ

structures based on $\langle 1/2\ 1/2\ 0 \rangle$ propagation vectors. Thus the method proposed in [4] could not be used for a complete determination of the field-induced $\langle 1/2\ 1/2\ 0 \rangle$ models.

To overcome this difficulty, we have developed some software to achieve a systematic search for the structures. Given four non-equivalent magnetic moments inside the magnetic cell, the four Fourier components are determined. By scanning all of the possible orientations for these four moments within the chosen family of high-symmetry directions ($\langle 100 \rangle$, $\langle 110 \rangle$ or $\langle 111 \rangle$), the complete set of field-induced high-symmetry structures could be established. The redundant cases were rejected by comparing the structures using the cubic point symmetry operations (phase domains were also detected). As a result of this procedure, 15 different field-induced structures were found for moments pointing along

⟨100⟩ directions, 35 for moments along ⟨111⟩ directions, and 128 for moments along ⟨110⟩ directions. All of them were used as models for comparison with the measured intensities.

3.1. The field along [0 0 1]

The purpose of these experiments was first to confirm the spontaneous structure as multiaxial, and second to access the maximum of field-induced phases, and reveal their respective magnetic structures. After demonstrating that no domain effects on the field dependence of the antiferromagnetic ⟨1/2 1/2 0⟩ reflections could be seen, numerous peaks were measured at $T = 10$ K and $H = 0$. To describe the absence of domain effects, the models for fitting these intensities have to be chosen from among the spontaneous structures preserving the cubic symmetry (i.e. which correspond to a single family of phase domains). From reference [4], only one set of three Fourier components can be retained, the resulting moments pointing along threefold directions. This set is reported in the first row of table 1, where it is associated with the sequence of propagation vectors giving the best reliability factor ($R = 6.84\%$). The moment amplitude resulting from the refinement is $|S| = 9.4$ μ_B, not far from the free-Dy-ion ground-multiplet value, which indicates the strength of the exchange field at $T = 10$ K, well below T_N.
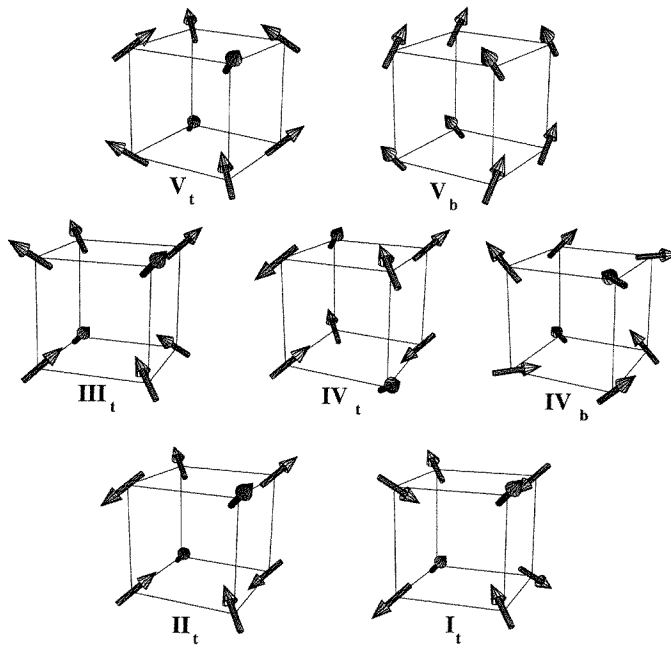

Figure 6. Magnetic structures associated with the phases stabilized for a fourfold direction of the applied magnetic field. Their labels refer to table 1, in which their Fourier description is detailed.

The real-space magnetic structure is represented in figure 6 (referred to as I_t, according to the label in table 1). From the quadrupolar point of view, this multiaxial structure is purely antiferroquadrupolar, the quadrupole components of the ε-representation being propagated by vectors which all belong to the ⟨1/2 1/2 0⟩ star. As discussed in reference [4], no macroscopic distortion is associated with such a structure, which agrees with the

spontaneous magnetostriction measurements [14].

Subsequent measurements have been carried out under an applied magnetic field of $\mu_0 H = 7.5$ T at $T = 2$ K, in phase II. For this field-induced structure, the systematic procedure described above has been used. The most satisfactory agreement was found for a four-Fourier-components structure with moments pointing along threefold directions (table 1, second row, and II_t in figure 6). Four domains had to be taken into account for the refinement, the reliability factor reaching 8.4%, the amplitude of the magnetic moment being 9.3 μ_B. Using the value of 9.3 μ_B for the moment amplitude, the magnetization for the undistorted state of the structure would be 2.7 μ_B, which is consistent with the magnetization curve at low temperature shown in reference [10]. Looking at the quadrupolar arrangement associated with this magnetic structure, it can be seen that the main quadrupolar Fourier components again have $\langle 1/2\ 1/2\ 0 \rangle$ propagation vectors, but, in contrast with the case of the spontaneous structure, there is here a small contribution from the zone centre associated with the trigonal ε-representation.

It should also be mentioned that another structure with moments pointing along twofold axes yields approximately the same reliability factor (8.1%) and moment amplitude (9.4 μ_B). The Fourier description of this model is

$$M_0 = [0\ -1/4\sqrt{2}\ 1/4\sqrt{2}] \qquad k_0 = [0\ 0\ 0]$$
$$M_1 = [1/\sqrt{2}\ 1/4\sqrt{2}\ -1/4\sqrt{2}] \qquad k_1 = [1/2\ 0\ 1/2]$$
$$M_2 = [0\ -1/4\sqrt{2}\ -1/4\sqrt{2}] \qquad k_2 = [1/2\ 1/2\ 0]$$
$$M_3 = [0\ 3/4\sqrt{2}\ 1/4\sqrt{2}] \qquad k_3 = [0\ 1/2\ 1/2].$$

However, for this structure of very low symmetry, not less than 16 domains have to be considered in the refinement. With so many free parameters in the refinement, this solution cannot be considered favourable in comparison with the previous one. In addition, when looking at the magnetization associated with this alternative model, one finds 1.7 μ_B for the component parallel to the [0 0 1] direction of the field. This value cannot be deemed satisfactory, in view of the magnetization curves of reference [10].

The following measurements for this fourfold direction of the applied field have been carried out on the D15 diffractometer at the ILL. In order to confirm the magnetic phase diagram obtained by magnetization measurements at temperatures near to T_N, in particular the border separating phases IV and V, the thermal dependencies of the [1/2 1/2 0], [−1/2 1 1/2], and [−1 −1/2 1/2] magnetic reflections have been measured for two magnetic field values, $\mu_0 H = 8.3$ T and $\mu_0 H = 7.8$ T. For $\mu_0 H = 8.3$ T (figure 7, upper part) the transition between phases V and IV is clearly manifested through the thermal evolution of the [1/2 1/2 0] reflection. While the intensities of both the [−1/2 1 1/2] and [−1 −1/2 1/2] reflections start increasing just below the paramagnetic–antiferromagnetic transition, the [1/2 1/2 0] reflection appears only when entering phase IV, at about $T = 52$ K. This reflection again disappears in phase III, and returns to measurable values in phase II. The $\mu_0 H = 7.8$ T measurements (figure 7, lower part) also confirm the transition line between phases IV and V. At this value of the field, consistently with the magnetization measurements, phase III cannot be reached, and, while decreasing the temperature, the last transition occurs between phases IV and II at $T = 41$ K. For each of these field values, the [−1/2 1 1/2] and [−1 −1/2 1/2] reflections show analogous behaviour, which simply reflects the equivalence of these vectors with respect to the [0 0 1] direction of the field (this cannot be taken as conclusive evidence as regards the symmetry properties of the [0 0 1] direction inside phases II, III, IV and V; even if not preserved, the
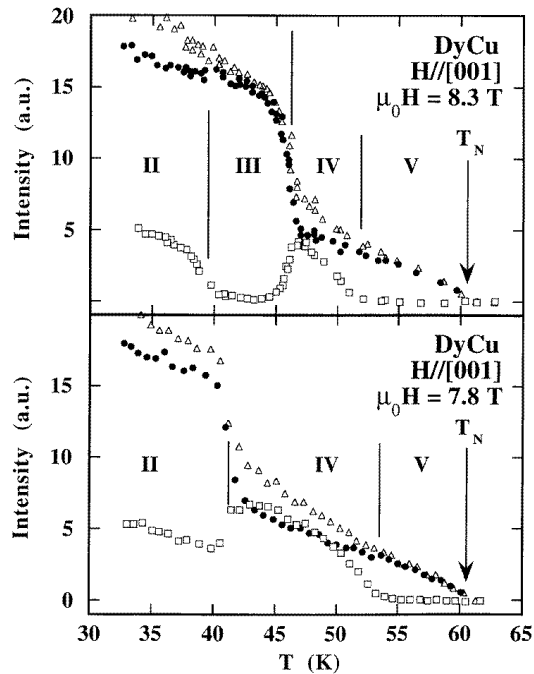
Figure 7. Thermal evolutions of the [1/2 1/2 0] (open squares), [−1/2 1 1/2] (open triangles), and [−1 −1/2 1/2] (black dots) magnetic reflections at $\mu_0 H = 7.8$ T and $\mu_0 H = 8.3$ T, the field being applied along [0 0 1]. The labels refer to the magnetic phases as indexed in figure 3.

fourfold symmetry could appear to be maintained owing to the sample partition into domains).

In the phase diagram for a field applied along [1 0 0] (figure 3), the locations of the transition points derived from the neutron diffraction measurements are reported as large circles. The detail of the intricate area of the diagram, around phase IV, is then confirmed by neutron diffraction.

The field being set at 8.3 T and the temperature at 44 K, in phase III, the intensities of numerous diffraction peaks were measured. All of the $\langle 1/2\ 1/2\ 0 \rangle$ field-induced structures were then used for fitting these intensities. The most satisfactory structure for phase III is described by three Fourier components, the resulting moments pointing along threefold directions (the third row in table 1). According to this structure, phase III is single domain (as already mentioned, phase domains are not considered). The resulting amplitude of the magnetic moment is 8.2 μ_B, the reliability factor being 11.4%. From the quadrupolar point of view, this structure, represented in figure 6 as III$_t$, is identical to the one associated with phase I (to visualize the quadrupolar arrangement associated with a magnetic structure, the simplest way is to consider the magnetic moments without their arrowheads). It is purely antiferroquadrupolar, with the three quadrupolar components of the ε-representation propagated by $\langle 1/2\ 1/2\ 0 \rangle$ vectors (AFQ ε).

At the same value of magnetic field, but for $T = 53$ K, an equivalent set of reflections has been measured inside phase V. As a result of the search for the structure fitting the measurements, two models with nearly equal reliability factors (11.3%) can be retained. The first one is again a structure with moments lying along threefold directions. The Fourier components are the same as for the structure found in phase III, the difference between

the two structures coming from the association with the propagation vectors (table 1, the penultimate row, and V_t in figure 6). Only one domain has to be considered, and, from the quadrupolar energy point of view, the structure is equivalent to the ones of phases I and III (AFQ ε).

In contrast, the second structure has no connection with what has been observed for the previously investigated phases. The moments directions are twofold, the structure being described by two Fourier components (table 1, last row, and V_b in figure 6). Two domains have to be considered for the refinement, each one introducing one family of $\langle 1/2\ 1/2\ 0 \rangle$ magnetic intensities. Looking at the quadrupolar aspect of the structure, quadrupolar components from the ε- and γ-representations are present, and respectively satisfy antiferroquadrupolar (AFQ ε) and ferroquadrupolar (FQ γ) interactions. No magnetization criterion can be of use in distinguishing the two models. At this temperature level, the magnetization curves (figure 1) show no well-defined anomaly, so no value for the magnetization of the undistorted structure can be unambiguously determined and compared with the last column of table 1.

For this fourfold direction of the field, phase IV was finally investigated at $T = 48$ K and $\mu_0 H = 8.3$ T. The neutron data are here less decisive in determining the corresponding magnetic structure. As a result of the testing of the high-symmetry models, not less than seven structures are found with reliability factors less than 15% (an arbitrary limit that we have defined because of the higher-than-average uncertainty in the peak intensities). We restrict ourselves to the best solutions found for twofold and threefold directions of the magnetic moments (respectively rows 4 and 5 in table 1, and IV_b and IV_t in figure 6). The solution with moments along twofold directions has the best reliability factor (10.8%); however, this results from a refinement involving eight domains. The ferromagnetic component is not parallel to the field, and, considering the smooth behaviour of the magnetization (figure 1), this structure should be strongly distorted (rotation of M_0), but with little effect on the antiferromagnetic components (M_1, M_2). From the quadrupolar point of view, this structure is compatible with antiferroquadrupolar interactions for the ε-representation and antiferroquadrupolar interactions for the γ-representation. The AFQ ε-representation aspect is common to all of the satisfactory structures found for this fourfold direction of the magnetic field. This is not the case for the AFQ γ-representation aspect, which is in conflict with the FQ γ-character of the other structure with the moment along $\langle 1\ 1\ 0 \rangle$, proposed for phase V.

The model retained for moments along threefold directions has a less good reliability factor (14.6 %). However, this was obtained after a refinement involving only four domains. Looking at the Fourier components of this model, one finds that they are identical with the ones for the structure found for phase II. The two structures differ only through the (k, M_k) association, and have then equivalent quadrupolar interaction energies [4]. They both satisfy AFQ ε-representation interactions.

3.2. The field along [1 1 1]

The spontaneous structure for this threefold direction of the magnetic field is obviously the same as the one observed for the fourfold direction. Only one structure had then to be determined for phase VI.

Using the same D15 diffractometer and cryomagnet, measurements for calibration were first done at zero field inside phase I. Subsequently, a wide collection of reflections were measured at $T = 40$ K and $\mu_0 H = 8.3$ T. After testing all of the high-symmetry field-induced structures, two satisfactory models were found with equivalent reliability factors,
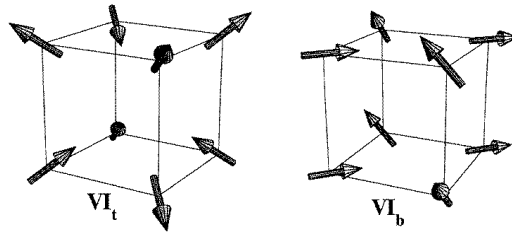
Figure 8. The two magnetic structures associated with the phase VI, stabilized for a magnetic field applied along a threefold direction. The labels refer to table 2, in which the Fourier descriptions are detailed.

$R = 7.6\%$.

One of the models consists of a structure with moments parallel to twofold axes, described in reciprocal space by four Fourier components (the second row in table 2, and VI_b in figure 8). Three domains have to be taken into account for the refinement. The amplitude of the magnetic moment being 8.1 μ_B, the projection of the ferromagnetic component along the direction of the applied magnetic field gives a magnetization of about 3.3 μ_B. Looking at the magnetization curves of figure 4, this appears to be in rather good agreement with the $T = 45$ K curve. Considering the associated quadrupolar arrangement, one finds that stabilizing this structure requires antiferroquadrupolar interactions for both the ε- and γ-representations.

The second satisfactory model is made up from moments along threefold directions. Four Fourier components are again involved in this structure (table 2, third row, and VI_t in figure 8), only one domain being needed for the refinement. The refined value for the amplitude of the moments is 8.5 μ_B, resulting in a magnetization of 4.25 μ_B. This value is higher than what can be evaluated from the $T = 45$ K curve of figure 4. However, due to the weak anisotropy displayed in that temperature range, one cannot definitely exclude this model on the basis of this magnetization criterion. Looking at the quadrupolar energy of this structure, one finds it identical to that of the spontaneous structure (pure AFQ ε).

4. Conclusion

The present work has determined the detailed $H–T$ phase diagrams of the compound DyCu for the main crystallographic directions of the applied field below $\mu_0 H = 16$ T. At low temperature, the isothermal magnetization curves show multistep processes, analogous to the ones observed for other rare-earth cubic compounds displaying multiaxial structures (as the main examples, NdZn [5], and TmGa$_3$ [15]). On increasing the temperature, these magnetization steps are progressively smoothed, the nature of some of the magnetic transitions becoming uncertain near to T_N. The analysis of the temperature dependence of the magnetization confirms the location of the transitions seen during the isothermal measurements, and gives more detail on the nearly vertical lines of the (H, T) phase diagrams. In particular, as a result of these isofield measurements, evidence for a new phase (V) just below T_N for a non-zero magnetic field applied along a fourfold direction has been obtained. This indicates an even more intricate nature of the (H, T) phase diagram for this field direction, which displays, within the measurement range, not less than five different phases. If one tries to explain the observed magnetic behaviour in terms of one-ion anisotropy and bilinear interactions, respectively favouring one unique family

Table 2. The Fourier description of the magnetic structures associated with the phases observed for a threefold direction of the field. The first column gives the conditions of the neutron diffraction measurements, and, in parentheses, the number of measured reflections. The labels refer to the real-space structures represented in figure 8. The fourth to sixth columns give respectively the number of domains involved in the refinement (N_{dom}), the reliability factor (R), and the amplitude of the moments ($|S|$). The seventh column gives the magnetization computed using $|S|$ for a rigid structure. The last column refers to the type of quadrupolar interaction compatible with the structure.

Phase	Magnetic structure		Label	N_{dom}	R (%)	$|S|$ (μ_B)	M (μ_B)	Inter-actions
I	$M_1 = [1/\sqrt{3}\ 0\ 0]$	$k_1 = [0\ 1/2\ 1/2]$	I_t	1	6.9	9.4 ± 0.2	0	AFQ ε
$T = 10$ K	$M_2 = [0\ 1/\sqrt{3}\ 0]$	$k_2 = [1/2\ 0\ 1/2]$						
$\mu_0 H = 0$ T	$M_3 = [0\ 0\ 1/\sqrt{3}]$	$k_3 = [1/2\ 1/2\ 0]$						
(28)								
VI	$M_0 = [1/4\sqrt{2}\ 1/4\sqrt{2}\ 1/2\sqrt{2}]$	$k_0 = [0\ 0\ 0]$	VI_b	3	7.6	8.1 ± 0.1	3.3	AFQ γ
$T = 40$ K	$M_1 = [3/4\sqrt{2}\ 3/4\sqrt{2}\ -1/2\sqrt{2}]$	$k_1 = [1/2\ 1/2\ 0]$						AFQ ε
$\mu_0 H = 8.3$ T	$M_2 = [1/4\sqrt{2}\ -1/4\sqrt{2}\ 0]$	$k_2 = [0\ 1/2\ 1/2]$						
(62)	$M_3 = [-1/4\sqrt{2}\ 1/4\sqrt{2}\ 0]$	$k_3 = [1/2\ 0\ 1/2]$						
	$M_0 = [1/2\sqrt{3}\ 1/2\sqrt{3}\ 1/2\sqrt{3}]$	$k_0 = [0\ 0\ 0]$	VI_t	1	7.6	8.5 ± 0.1	4.25	AFQ ε
	$M_1 = [1/2\sqrt{3}\ 1/2\sqrt{3}\ -1/2\sqrt{3}]$	$k_1 = [1/2\ 1/2\ 0]$						
	$M_2 = [-1/2\sqrt{3}\ 1/2\sqrt{3}\ 1/2\sqrt{3}]$	$k_2 = [0\ 1/2\ 1/2]$						
	$M_3 = [1/2\sqrt{3}\ -1/2\sqrt{3}\ 1/2\sqrt{3}]$	$k_3 = [1/2\ 0\ 1/2]$						

of crystallographic directions for the moments and one unique star of antiferromagnetic propagation vectors, some transition lines have unexpected aspects. Within these simple hypotheses, in the case of a second-order transition at T_N, one would expect the transition lines associated with the magnetization steps to uniformly converge, with a negative slope, towards the (T_N, $H = 0$) point. This can be easily interpreted if one considers that the bilinear interaction energy behaves as the square of the antiferromagnetic order parameter, while the Zeeman term is linear both in magnetic field and order parameter. For a magnetic field applied along a fourfold direction of DyCu, the lines between phases II and IV, III and V, and, to a lesser extent, I and II, show positive slopes. This gives additional evidence of the non-trivial kind of interaction involved in the magnetic order range of this compound.

The phase diagram for a threefold direction of the field displays only two phases, but the single transition line, between phases I and VI, also has an intriguing aspect. The associated critical field has a nearly constant value over the whole temperature range, as opposed to the expected convergence of the transition line towards T_N. In addition, the nature of that transition is difficult to define: it is clearly of first order at low temperatures where a sharp magnetization step is observed, but the amplitude of the step cancels close to T_N.

For a magnetic field applied along a twofold direction, only magnetization measurements have been carried out. They reveal a phase diagram that is apparently more complex than the one observed for a threefold direction, but similar to the one for the fourfold direction.

For all of the phases investigated, a satisfactory fitting of the neutron diffraction results has been obtained. As a consequence of the existence of numerous high-symmetry models for a $\langle 1/2\ 1/2\ 0 \rangle$ antiferromagnetic star, alternative models do exist for the structures associated with phases IV, V, and VI. The ambiguity may be removed within hypotheses

involving the quadrupolar interactions and the easy axes.

Assuming the easy axes to be threefold over the whole order range, all of the magnetic structures determined respect the same condition on the quadrupolar interactions, which have to be antiferroquadrupolar for the ε-representation (i.e. $K^\varepsilon(1/2\ 1/2\ 0) > K^\varepsilon(0)$). The sequence of the structures would be then consistent within the framework of the quadrupolar interactions model. However, the positive temperature slope of some of the transition lines of the diagrams would remain unexplained, as would the transition between phases III and V. This latter would then correspond to a change in the association between the Fourier components and the propagation vectors of the structure: within a model based on bilinear interactions, one-ion anisotropy, and quadrupolar interactions, these two phases would have exactly the same energy. Actually, no energy term involves the relative layout of the M_k Fourier component with its propagation vector k.

If one accepts a change from threefold to twofold easy axes inside the magnetic order range, some of the difficulties in interpreting the phase diagrams may be resolved. As already observed for the compound NdZn, an (H, T) transition line separating phases with different easy axes can have a positive slope. However, if all of the selected structures (in tables 1 and 2) with moments along twofold axes are retained, inconsistencies are revealed by the analysis of the quadrupolar interactions. Although all of the structures are then antiferroquadrupolar for the ε-representation, for the γ-representation, the structures IV_b and VI_b are antiferroquadrupolar when structure V_b is ferroquadrupolar. Excluding the structure V_b in favour of structure V_t reintroduces the difficulty of interpreting the positive slope of the III–V transition line.

At this stage, the maximum information has been derived from the magnetization and neutron diffraction measurements. Numerical calculations using the periodic field method are expected to clarify some of the reported ambiguities. In particular, the occurrence of a change of easy axes, under an applied magnetic field, can be checked as consistent or not with the presumed CEF scheme. This approach, including quadrupolar interactions, has already been successfully used in the case of the compound NdZn [6]. It would be of considerable interest to check whether the model is valid for the general case of rare-earth cubic compounds or, on the other hand, to demonstrate the need for additional couplings in certain cases.

References

[1] Coqblin B 1977 *The Electronic Structure of Rare-earth Metals and Alloys: the Magnetic Heavy Rare Earths* (New York: Academic)
[2] Morin P and Schmitt D 1990 *Ferromagnetic Materials 5* ed K H J Buschow and E P Wohlfarth (Amsterdam: North-Holland) p 1
[3] Morin P, Rouchy J and Schmitt D 1978 *Phys. Rev.* B **17** 3684
[4] Amara M and Morin P 1995 *Physica* B **205** 379
[5] Amara M, Morin P and Burlet P 1995 *Physica* B **210** 157
[6] Amara M and Morin P 1996 *Physica* B **222** 61
[7] Wintemberger M and Chamard-Bois R 1972 *Acta Crystallogr.* A **28** 341
[8] Rossat-Mignod J 1986 *Neutron Scattering in Condensed Matter Research* ed K Sköld and D L Price (New York: Academic)
[9] Wintemberger M, Chamard-Bois R, Belakhovsky M and Pierre J 1971 *Phys. Status Solidi* b **48** 705
[10] Aléonard R, Morin P and Rouchy J 1984 *J. Magn. Magn. Mater.* **46** 233
[11] Amara M, Morin P and Voiron J 1995 *Physica* B **211** 152
[12] Stassis C, Deckman H W, Harmon B N, Desclaux J P and Freeman A J 1977 *Phys. Rev.* B **15** 369
[13] Amara M, Galéra R M, Morin P, Voiron J and Burlet P 1994 *J. Magn. Magn. Mater.* **131** 402
[14] Morin P and Pierre J 1974 *Phys. Status Solidi* b **21** 161.
[15] Morin P, Giraud M, Burlet P and Czopnik A 1987 *J. Magn. Magn. Mater.* **68** 107